

Tailoring of a Visible-Light-Absorbing Biaxial Ferroelectric towards Broadband Self-Driven Photodetection

Shiguo Han

Fujian Institute of Research on the Structure of Matter, Chinese Academy of Sciences

Maofan Li

Fujian Institute of Research on the Structure of Matter

Yi Liu

Fujian Institute of Research on the Structure of Matter

Wuqian Guo

State Key Laboratory of Structural Chemistry, Fujian Institute of Research on the Structure of Matter, Chinese Academy of Sciences;

Mao-Chun Hong

State Key Laboratory of Structure Chemistry, Fujian Institute of Research on the Structure of Matter, Chinese Academy of Sciences.

Zhihua Sun

Fujian Institute of Research on the Structure of Matter

Junhua Luo (✉ jhluo@fjirsm.ac.cn)

State Key Laboratory of Structural Chemistry, Fujian Institute of Research on the Structure of Matter, Chinese Academy of Sciences;

Article

Keywords: ferroelectric, photodetection, bulk photovoltaic effects

Posted Date: August 31st, 2020

DOI: <https://doi.org/10.21203/rs.3.rs-63156/v1>

License:   This work is licensed under a Creative Commons Attribution 4.0 International License.

[Read Full License](#)

Version of Record: A version of this preprint was published at Nature Communications on January 12th, 2021. See the published version at <https://doi.org/10.1038/s41467-020-20530-4>.

Abstract

In term of strong light-polarization coupling, ferroelectric materials with bulk photovoltaic effects (BPVEs) afford a promising avenue for newly-conceptual optoelectronic devices. However, due to severe polarization deterioration caused by leakage current of photoexcited carriers, most of ferroelectrics are merely capable of absorbing 8 ~ 20% of visible-light spectra. BPVE-active ferroelectrics with the narrow bandgap ($E_g < 2.0$ eV) are still scarce, hindering their practical applications. Here, we present a new 2D lead-iodide hybrid biaxial ferroelectric, $[(\text{CH}_3)_2\text{CH}(\text{CH}_2)_2\text{NH}_3]_2(\text{CH}_3\text{CH}_2\text{NH}_3)_2\text{Pb}_3\text{I}_{10}$ (**1**), which shows large spontaneous polarization ($P_s = 5.2 \mu\text{C}/\text{cm}^2$) and the narrow direct bandgap ($E_g = 1.80$ eV). To the best of our knowledge, this E_g value of **1** is the smallest figure ever observed for the existing molecular ferroelectrics. Particularly, the symmetry breaking of $4/mmmFmm2$ species results in its biaxial attributes, that is, four equivalent P_s directions for **1**. Accordingly, exceptional in-plane BPVEs are exploited along the crystallographic [001] and [010] axes directions inside the crystallographic bc -plane, of which the directions can be facily switched through external electric poling. At zero bias, the intriguing self-driven photoactivities were created in a wide range of 365–670 nm, including large switching ratio ($> 10^5$), high-density photocurrent ($\sim 1.5 \mu\text{A}/\text{cm}^2$) and ultrafast transient responding time (~ 2.7 ns). It is the coupling between ferroelectricity and in-plane BPVEs that endows great potentials of **1** toward broadband self-driven photodetection. This innovative study on in-plane ferroelectric BPVEs is unprecedented, which sheds light on new properties for their future optoelectronic device applications.

Introduction

Bulk photovoltaic effects (BPVE) of ferroelectric materials is a strong light-polarization coupling with unique physical attributes,^{1–4} including ultrahigh anomalous photovoltage, polarization-dependent activity and steady-state photocurrent in a homogeneous media, *etc.* In contrast to conventional asymmetric systems of Schottky barrier and p - n junction,⁵ these merits of ferroelectrics are closely related to spontaneous polarization (P_s), which creates an internal electric field at least one order of magnitude higher than that in the p - n junction.⁶ The strong electric field allows efficient dissociation of photogenerated charge carrier and further leads to large non-zero shift photocurrents.⁷ That is, without an external source, a controllable power supply can be expected in BPVE-active ferroelectrics, which offers an avenue for assembling the newly-conceptual photoelectronic devices (*e.g.* self-driven photodetector).^{8–10} Currently, the mainstream of ferroelectric oxides still suffer from wide bandgap (E_g), such as BaTiO_3 (~ 3.2 eV), LiNbO_3 (~ 3.6 eV), BiFeO_3 (~ 2.7 eV) and $\text{Pb}(\text{Zr,Ti})\text{O}_3$ (~ 3.6 eV); this suggests only 8 ~ 20% of solar spectrum can be absorbed, greatly hindering their broadband device applications.¹¹ Although photovoltaic effects in ferroelectrics have been known for more than 60 years, BPVE-active ferroelectrics with the E_g smaller than 2.0 eV remain scarce. In this context, significant endeavors should be focused on exploring the visible-light-absorbing ferroelectric candidates with strong BPVEs, because the current leakage of photoexcited charge carriers will cause severe deterioration of electric polarization.

Two-dimensional (2D) hybrid perovskites with the formula of $(A^{\oplus})_2(A)_{n-1}M_nX_{3n+1}$, where A^{\oplus} and A are organic cations, M is metal and X is halogen, are booming as a new class of optoelectronic materials.¹² In contrast to the 3D AMX_3 prototype subject to the Goldschmidt's tolerance factor, this 2D branch exhibits infinite structural flexibility and tunability. It should be emphasized that, if the flexible aliphatic organic spacer (A^{\oplus}) is adopted, a large degree of molecular freedom for dynamic motions tends to trigger phase transition and favor the generation of ferroelectricity.^{13,14} Further, a delicate bandgap engineering can be performed by tailoring thickness of inorganic sheets (the n value) and/or modifying halogen (X), which possibly fulfills the target of narrow bandgap.^{15,16} Of special concern is the 2D lead-iodide counterparts that combine robust ferroelectricity and exotic visible-light-absorbing capacity, affording opportunities to explore new BPVE-active ferroelectrics. For instance, a few 2D lead-iodide ferroelectrics, such as (4,4-difluorocyclohexylammonium)₂PbI₄ and [4-(aminomethyl) piperidinium]₂PbI₄ have been recently reported.^{17,18} Nevertheless, owing to the monolayered inorganic perovskite sheets ($n = 1$), they still possess the relatively wide bandgap ($E_g > 2.3$ eV) along with the lacking of ferroelectric BPVEs. One effective pathway is to increase thickness of inorganic sheets (the n value) while retaining ferroelectricity of 2D lead-iodide hybrid perovskites. Consequently, we attempted to perform structure tailoring to balance the ferroelectricity and optical absorption, which is not only crucial for exploring new BPVE-active ferroelectrics but also for deepening the understanding on relationship between electric polarization and BPVEs.

We here present a new visible-light-absorbing biaxial ferroelectric in the family of 2D hybrid perovskites, (isopentylammonium)₂(ethylammonium)₂Pb₃I₁₀ (**1**), which has a large P_s value of 5.2 $\mu\text{C}/\text{cm}^2$ and the narrowest direct bandgap ($E_g = 1.8$ eV) for the molecular ferroelectrics. Most notably, exceptional in-plane BPVEs are observed along its crystallographic [001] and [010] axes inside the bc -plane, stemming from its biaxial ferroelectricity. Such unique BPVEs allow the broadband self-driven photoactivities of **1** in the wide range of 365–670 nm, showing the high-density photocurrents (1.5 $\mu\text{A}/\text{cm}^2$) and large switching ratio ($> 10^5$). This work paves a pathway for the design of photoferroelectric materials, and expanding their desirable properties for newly-conceptual optoelectronic device applications.

Results And Discussion

High-quality dark red crystals of **1** were grown by the temperature cooling method (Figure S1), and the phase purity has been confirmed by powder X-ray diffraction (Figure S2). Preliminary differential scanning calorimetry (DSC) measurements display two pairs of the exothermic/endothemic peaks in the cooling/heating modes (Fig. 1a), suggesting the occurrence of successive reversible phase transitions. Our subsequent studies disclose that **1** undergoes the ferroelectric-to-antiferroelectric phase transition ($T_1 = 313$ K), and antiferroelectric-to-paraelectric phase transition ($T_2 = 340$ K), respectively. For convenience, we label the three phases of **1** as: ferroelectric phase (FEP, below T_1); antiferroelectric phase (AFEP, between T_1 and T_2), and paraelectric phase (PEP, above T_2). Moreover, since dielectric constant (ϵ^{\oplus}) is closely related to the degree of the electric polarizability, the successive phase transitions in **1** were

solidly confirmed by the noticeable anomalies of its temperature-dependent dielectric constants. Figure 1b depicts two different type of dielectric anomalies observed in **1**; the sharp dielectric peaks at T_2 suggest its order-disorder structure change, while the step-like anomaly at T_1 should relate to the reorientation of molecular dipoles.

Variable-temperature crystal structures of **1** were determined by single-crystal X-ray diffraction to deeply probe its phase transition mechanism. At the FEP, it crystallizes in the orthorhombic system with space group $Cmc2_1$ (polar point group $mm2$, Table S1). General structure of **1** adopts a typical 2D Ruddlesden-Popper motif, with an alternative arrangement of inorganic trilayered perovskite frameworks containing $\{Pb_3I_{10}\}_n$ and organic bilayers of isopentylammonium spacer. As shown in Fig. 2a, the inorganic sheets are perpendicular to its crystallographic $\langle 100 \rangle$ direction, termed as the $\langle 100 \rangle$ -oriented family. Notably, organic ethylammonium cation is tightly confined inside the cavity enclosed by the corner-sharing PbI_6 octahedra *via* strong N-H...I hydrogen bonds (Figure S3). All perovskite trilayers of $\{Pb_3I_{10}\}_n$ distribute inside the *bc*-plane and form almost equivalent packings along its [001] and [010] directions, of which the in-plane structural isotropy leads to its biaxial ferroelectricity and in-plane BPVEs. Specially, the incorporation of large-size ethylammonium cation into the perovskite cages suggests severe distortion of PbI_6 octahedra, as deduced by the I-Pb-I angles and Pb-I lengths (Tables S2 and S3). This distorted geometry of PbI_6 octahedra greatly favors the generation of electric polarization. Moreover, organic bilayers of isopentylammonium cations are situated in the interlayer space and linked to inorganic sheets by N-H...I bond (Figure S4). The head-to-tail arrangement involves that two adjacent layers of spacer cations are staggered to each other with a (1/2 1/2) shift. Molecular dynamics simulation and proton NMR have evidently revealed the fast dynamic motions of organic cations at A and A' sites afford the driving force to trigger phase transition and ferroelectric polarization, as verified by other 2D ferroelectrics, such as $(BA)_2CsPb_2Br_7$ and $(BA)_2(\text{formamidinium})_2Pb_3Br_{10}$,^{19,20} *etc.*

With the temperature increasing between T_1 and T_2 , crystal structure of **1** belongs to the nonpolar space group of $Pm\bar{c}n$ (the point group mmm). Its perovskite structural motif is still identified as an octahedral tilting architecture, which results in the emergence of local polarization. However, distinct from its ferroelectric state, an antiparallel alignment is assumed to satisfy the requirement of crystallographic symmetry for antiferroelectric order. For instance, both isopentylammonium and ethylammonium cations in the unit cell exhibit two orientations, as revealed by the arrowheads in Figure S5. Symmetry-related moieties in the neighboring slab displace in exactly the opposite directions with the same magnitude, cancelling out net polarization of the unit cell. Accordingly, the tilting of PbI_6 octahedra also occurs, as verified by the off-center displacements of Pb ions. Such a collaboration gives rise to antiparallel dipole arrangement for **1**, along with the elimination of net electric polarization at AFEP (*i.e.* $P_s = 0$). Further heating beyond T_2 , **1** transforms to the tetragonal system with a nonpolar space group of $I4/m\bar{m}m$ (the point group of $4/m\bar{m}m$). The characteristic is that both organic isopentylammonium and ethylammonium cations become highly disordered and locate on the crystallographic mirror plane (Figure S6); all the inorganic PbI_6 octahedra feature a highly-symmetric configuration. This centrosymmetric

packing totally eliminates the polarization of **1**, corresponding to its paraelectric state. Thus, symmetry breaking of $4/mmmFmm2$ can be deduced at T_1 , which belongs to one of the 88 species for ferroelectrics and reveals multiaxial nature for **1**.²¹ That is, the polarized direction of **1** is confined along crystallographic c -axis at FEP, coinciding with the [110]-direction at PEP (Fig. 2b). Due to four equivalent [110]-directions at PEP, four equivalent polarization-directions can be verified for **1** (Fig. 2c); this multiaxial attribute is also confirmed by the P - E hysteresis loops measured along the different directions.

Second harmonic generation (SHG) technique has been developed as an effective tool to detect symmetry breaking in ferroelectrics.²² Here, variable-temperature SHG properties were studied during the successive phase transitions of **1**. Figure 3a depicts that **1** is SHG-active at FEP (below T_1); with temperature rising, its SHG signal exhibits a gradual decline and becomes basically unresponsive above the T_1 . This obvious change of SHG effects behaves as a direct proof to symmetry breaking in **1**. During its FEP-to-PEP phase transition, the sharp pyroelectric current peak in the vicinity of T_1 is reminiscent of electric polarization, and the optimum P_s is estimated to be $5.2 \mu\text{C}/\text{cm}^2$ (Fig. 3b). As the most direct evidence of ferroelectricity, the well-shaped rectangular P - E hysteresis loops were recorded at 298 K using the Sawyer-Tower circuit method. At the frequency of 25 Hz, the P - E loop affords the saturated P_s value of $5.0 \mu\text{C}/\text{cm}^2$ and the coercive electric field (E_c) of 9 kV/cm, respectively (Fig. 3c). These figure-of-merits fall in the range of some other organic-inorganic hybrid ferroelectrics, such as TMCM-MnCl₃.²³ Emphatically, such perfect rectangular P - E hysteresis loops can be facilely achieved not only along the b^{FEP} -axis direction, but also along the crystallographic c^{FEP} -axis. As shown in Fig. 3c, the experimental P - E hysteresis loops have the almost identical motifs, suggesting the biaxial merit of ferroelectricity in **1**. That is, its electric polarization can be switched along two axes with four equivalent directions. In terms of our structure analyses on its symmetry breaking, it is the in-plane structural isotropy of the crystallographic bc -plane that results in equivalent packings along the b - and c -axes, as well as biaxial ferroelectricity of **1**. All these findings illuminate that **1** is a room-temperature biaxial ferroelectric material, which should be a potential candidate for exploiting the in-plane BPVEs. Besides, the antiferroelectric attribute of **1** is also validated by the double P - E hysteresis loop at AFEP (325 K), while the linear straight line discloses its paraelectric feature above the T_2 (Fig. 3d).

For ferroelectric materials, it is an intrinsic contradiction between superior excellent ferroelectricity and narrow optical bandgap; that is, leakage current caused by the increasing of photoexcited carriers would result in the deterioration of polarization.²⁴ The most of oxide ferroelectrics, such as BaTiO₃, P(Zr,Ti)O₃ and BiFeO₃, suffer from their wide bandgap in the range of 2.7 ~ 4 eV, which enable the usage of only 8–20% of solar spectrum.^{11,25,26} Here, the sharp absorption edge at 670 nm and PL peak at 603 nm are observed for **1**, of which the E_g is estimated as 1.82 eV based on the $Tauc$ equation (Fig. 4a). First-principle calculations on the electronic structure disclose that the conduction band minimum (CBM) and valence band maximum (VBM) of **1** coherently locate at the G point, indicating its direct-bandgap feature, and the calculated E_g of 1.80 eV coincides with our experimental result (Fig. 4b). As far as we know, **1** has the narrowest bandgap for molecular ferroelectrics (Table S5), much smaller than those of other lead-

iodide ferroelectrics, such as (4,4-difluorocyclohexylammonium)₂PbI₄ (~ 2.38 eV),¹⁷ [4-(aminomethyl)-piperidinium]₂PbI₄ (~ 2.38 eV),¹⁸ [(CH₃)₃NCH₂I]PbI₃ (~ 2.82 eV), R- and S-1-(4-chlorophenyl)-ethylammonium]₂PbI₄ (~ 2.34 eV),^{27,28} *etc.* This result well balances the contradiction between ferroelectricity and optical absorption, which endows strong light-polarization coupling and remarkable photoactivities. Further analyses on charge-density distributions in-plane disclose that the charge density of CBM and VBM originates from Pb *s*, Pb *p* and I *p* states in the inorganic *bc*-plane sheets (Fig. 4c). The almost isotropy of charge-density distributions in the (100) plane result in its biaxial ferroelectricity and in-plane BPVEs. For the VBM, the strong antibonding coupling of Pb *s* and I *p* states favors a small hole effective mass comparable with electron effective mass.²⁹ Generally, charge transport dynamics of materials are essential for their semiconducting properties. Current-voltage (*I-V*) response followed by space charge limited current (SCLC) analysis was measured to validate the transport properties of crystal **1**. Figure 4d shows that the logarithmic *I-V* trace has two different regimes: ohmic region (*n* = 1) and trap-filled limited (TFL) regime (*n* > 3). The drift mobility is extracted to be 0.5 cm² V⁻¹ s⁻¹, much larger than that of other ferroelectrics, indicating excellent semiconductor properties of **1**.

The notable biaxial ferroelectricity and excellent semiconducting feature along the (100) plane of **1** offer great opportunities to obtain the in-plane BPVEs. Short-circuit photocurrent (*I_{sc}*) were measured on surface of **1** under incident illumination of 637 nm without the bias voltage applied (Fig. 5a). More specifically, in order to explore the polarization-induced BPVEs, lateral-type gold electrodes were fabricated aligned parallel/perpendicular to the direction of (100) plane. As shown in Fig. 5b, for the electrodes aligning in the (100) plane (A1 and A2), prominent *I_{sc}* (~ 6 nA) were observed under the incident illumination intensity of 30 mW/cm². However, for the electrodes aligning perpendicular to the direction of (100) plane (A3), no *I_{sc}* signal could be detected (the bottom of Fig. 5b). That is, exceptional in-plane ferroelectric BPVEs are exploited in the (100) plane. As far as we are aware, the ferroelectric polarization-induced electric field of (100) plane plays an important role in such interesting phenomenon. From another point of view, the evident symmetry breaking with 4/*mmmFmm2* species of **1** result in two equivalent polar axes (*b*-axis and *c*-axis). Then, the in-plane BPVE of **1** are closely related to its ferroelectric polarization-induced electric field of (100) plane.

In principle, ferroelectrics with BPVE cloud offer the power supply for itself. Based on such excellent in-plane BPVE, **1** could behave as a promising candidate for broadband polarization self-driven photodetection. As shown in Fig. 6a, *I-V* measurements were performed along the *b*-, *c*- and *a*-axis, respectively. The obvious polarization self-driven effects are easily obtained along the *b*-, *c*-axis, including zero-bias *I_{sc}* and open circuit voltage (*V_{oc}*). However, there is no *I_{sc}* and *V_{oc}* signal along the *a*-axis (Insert of Fig. 6a). That is, self-driven photodetection behaviors should be only exploited along the *b*- and *c*-axis direction. This behavior is well consistent with the in-plane (100) BPVE of **1**. Figure 6b presents the photocurrent density dependence of voltage bias of **1** illuminated with a 637 nm laser along the polar axis direction. Specifically, under illumination of 127 mW/cm², the zero-bias *I_{sc}* and *V_{oc}* measured to be ~ 1.5 μA/cm² and ~ 0.8 V, respectively. Such short circuit current is slightly larger than the most active

ferroelectric oxide BiFeO₃ ($\sim 0.4 \mu\text{A}/\text{cm}^2$),³⁰ and superior to those of some ferroelectric oxides, such as [KNbO₃]_{1-x}[BaNi_{1/2}Nb_{1/2}O_{3- δ}]_x ($\sim 0.1 \mu\text{A}/\text{cm}^2$) under the halogen lamp ($\sim 4 \text{mW}/\text{cm}^2$), (Pb, La)(Zr,Ti)O₃ ($8 \text{nA}/\text{cm}^2$) and (Na,K)NbO₃ ($\sim 25 \text{nA}/\text{cm}^2$) under ultraviolet illumination.^{31,32} In addition, the dark current ($I_{\text{dark}} \sim 1 \times 10^{-14} \text{A}$) is lower at least by 2 orders than reported traditional *p-n* based devices.³³ Such extremely low I_{dark} and considerable I_{sc} generate a large switching ratio of 10^5 at the zero bias, which indicates the excellent self-driven photodetection properties of **1**. Besides, the transient response speed of **1** can reach to the nanosecond level (~ 2.7 and $\sim 3.8 \text{ns}$) under a nano-second laser illumination (Fig. 6c). Such ultrafast response reveals the rapid carrier recombination process and low electron-hole pair transit time, which could broaden the application scope of photoelectric devices. Moreover, the wavelength-dependent I_{sc} of **1** was carried out ranging from 365 to 940 nm. As shown in Fig. 6d, **1** exhibits obvious I_{sc} signal in the wide range of 365–670 nm, which is consistent with its narrow optical absorption bandgap. Compared to traditional inorganic materials, such as ZnO,⁹ BiFeO₃,³⁴ Pb(Zr,Ti)O₃³⁵ and GaN,³⁶ **1** possesses the wider self-driven detection range up to 670 nm. As far as we know, this figure-of-merit is the widest value obtained for the existing molecular ferroelectrics materials, which endows great potentials of **1** toward broadband self-driven photodetection.

Particularly, with the temperature increasing, the circuit voltage decreases gradually and disappears completely above the T_1 (Fig. 7a). This tendency coincides with that of the temperature-dependent polarization (Fig. 3b), being reminiscent of the close relationship with its ferroelectricity. We further studied the switching of photovoltage after application of 1500 V voltage pulses to the device. It is obvious that both the direction of V_{oc} and I_{sc} can be reversed by inverting electric poling, while the magnitude keeps almost unchanged (Fig. 7b). Such a flipping of photo-induced voltage and current attribute to the direction change of electric polarization in **1**, which has been verified in ferroelectrics of BiFeO₃ and PLZT ceramics.³¹ The origin of BPVE in ferroelectrics has been extensively studied and some speculative models were also suggested on inorganic materials, such as the depolarization-dependent band bending at metal-ferroelectric interface, asymmetry potentials related to the depolarization field, and nonlinear optical-rectification effect, *etc.*³⁷⁻⁴⁰ As far as we are aware, all these scenarios state that polarization makes a critical role to BPVE. In this regard, the sign of photocurrent and photovoltage can be reversed by inverting poling, which involves with the switching of polarization. Here, it is supposed that photocurrent switching of **1** also involves with the separation and flipping of polarization-related photoexcited carriers (Fig. 7c). For **1**, the dynamic motions of organic moieties are restrained with temperature lowering below the T_1 . From a structural point of view, this preferred orientation of organic cations results in the breaking of its prototypic mirror symmetry, and thus creates a degree of long-range dipolar order. Besides, the inorganic framework of **1** is also strongly influenced by the molecular orientation. Therefore, the electric switching and temperature-dependence of the BPVE behavior confirms the role of ferroelectricity in **1**, which stems from the dynamic reorientation of organic cations and tilting motions of inorganic Pbl₆ octahedra.

In summary, we have successfully reported a new visible-light-absorbing molecular ferroelectric: (isopentylammonium)₂(ethylammonium)₂Pb₃I₁₀ (**1**), which possesses the narrowest bandgap ~ 1.80 eV for the molecular systems. Emphatically, **1** exhibits exceptional in-plane BPVEs in the (100) plane, stemming from its bi-axial ferroelectricity. Such BPVE activities and narrow bandgap endow intriguing self-powered photoactivities in a broadband range of 365–670 nm, which far more superior than conventional perovskite structural metal oxides. Without external energy source, **1** creates switchable photovoltaic current with high current density ($\sim 1.5 \mu\text{A}/\text{cm}^2$) and large switching ratio ($> 10^5$), far beyond the most active oxide counterpart of BiFeO₃. Structural analyses reveal that this unique self-driven photodetection behavior of **1** stem from dynamic ordering of organic cations, along with the tilting motion of inorganic Pbl₆ octahedra. Our work allows for a deep understanding on the origin of ferroelectric self-powered photodetection effects, and will undoubtedly promote their further optoelectronic application potentials.

Declarations

Data availability.

The structures have been deposited at the Cambridge Crystallographic Data Centre (deposition numbers: CCDC 1950869, 1950872 and 1950875), and can be obtained free of charge from the CCDC via www.ccdc.cam.ac.uk/getstructures.

Competing financial interests

The authors declare no competing financial interests.

Author contributions

S.G.H prepared the samples and wrote the manuscript. M.F.L determined the structures. Y.L and W.Q.G. measured the ultraviolet-visible absorption spectroscopy. J.H.L and Z.H.S designed and directed the studies. All authors contributed to write and review the manuscript.

Acknowledgements

This work was supported by National Natural Science Foundation of China (21875251, 21833010, 21525104 and 21921001), the Key Research Program of Frontier Sciences of the Chinese Academy of Sciences (ZDBS-LY-SLH024), the NSF of Fujian Province (2018H0047), the Strategic Priority Research Program of the CAS (XDB20010200), and Youth Innovation Promotion of CAS (2019301 and 2020307).

References

1. Scott, J. F. & Paz de Araujo, C. A. Ferroelectric Memories. *Science* 246, 1400–1405 (1989).
2. Spaldin, N. A. & Fiebig, M. The Renaissance of Magnetoelectric Multiferroics. *Science* 309, 391–392 (2005).
3. Kreisel, J. et al. A Photoferroelectric Material is More Than the Sum of its Parts. *Nat. Mater.* 11, 260 (2012).
4. Lu, H. et al. Mechanical Writing of Ferroelectric Polarization. *Science* 336, 59–61 (2012).
5. Yang, S. Y. et al. Above-Bandgap Voltages from Ferroelectric Photovoltaic Devices. *Nat. Nanotechnol.* 5, 143–147 (2010).
6. Lejman, M. et al. Giant ultrafast photo-induced shear strain in ferroelectric BiFeO₃. *Nat. Commun.* 5, 4301 (2014).
7. Glass, A. M. et al. High-Voltage Bulk Photo-voltaic Effect and the Photorefractive Process in LiNbO₃. *Appl. Phys. Lett.* 25, 233 (1974).
8. Peng, L. et al. Energy Harvesting for Nanostructured Self-Powered Photodetectors. *Adv. Funct. Mater.* 24, 2591–2610 (2014).
9. Xu, S. et al. Self-Powered Nanowire Devices. *Nature Nanotechnology.* 5, 366–373 (2010).
10. Park, S. G. et al. Self-Powered Ultra-Flexible Electronics via Nanograting-Patterned Organic Photovoltaics. *Nature* 561, 516–521 (2018).
11. Grinberg, I. et al. Perovskite Oxides for Visible-Light-Absorbing Ferroelectric and Photovoltaic Materials. *Nature* 503, 509–512 (2013).
12. Blancon, J. C. et al. Extremely Efficient Internal Exciton Dissociation Through Edge States in Layered 2D Perovskites. *Science* 355, 1288–1292 (2017).
13. Mitzi, D. B. et al. Conducting Tin Halides with A Layered Organic-Based Perovskite Structure. *Nature* 369, 467–469 (1994).
14. Kagan, C. R. et al. Organic-Inorganic Hybrid Materials as Semiconducting Channels in Thin-Film Field-Effect Transistors. *Science* 286, 945–947 (1999).
15. Smith, I. C. et al. A Layered Hybrid Perovskite Solar-Cell Absorber with Enhanced Moisture Stability. *Angew. Chem. Int. Ed.* 53, 11232–11235 (2014).
16. Cortecchia, D. et al. Broadband Emission in Two-Dimensional Hybrid Perovskites: The Role of Structural Deformation. *J. Am. Chem. Soc.* 139, 39–42 (2017).
17. Sha, T. T. et al. Fluorinated 2D Lead Iodide Perovskite Ferroelectrics. *Adv. Mater.* 31, 1901843 (2019).
18. Park, I. H. et al. Ferroelectricity and Rashba Effect in a Two-Dimensional Dion-Jacobson Hybrid Organic-Inorganic Perovskite. *J. Am. Chem. Soc.* 141, 15972–15976 (2019).
19. Li, L. N. et al. Bilayered Hybrid Perovskite Ferroelectric with Giant Two-Photon Absorption. *J. Am. Chem. Soc.* 140, 6806–6809 (2018).
20. Wu, Z. Y. et al. Alloying n-Butylamine into CsPbBr₃ To Give a Two-Dimensional Bilayered Perovskite Ferroelectric Material. *Angew. Chem. Int. Ed.* 57, 8140–8143 (2018).

21. Aizu, K. Possible Species of Ferromagnetic, Ferroelectric, and Ferroelastic Crystals. *Phys. Rev. B*, 2, 754–772 (1970).
22. Shi, P. P. et al. *Chem. Soc. Rev.* 45, 3811–3827 (2016).
23. You, Y. M. et al. An Organic-Inorganic Perovskite Ferroelectric with Large Piezoelectric Response. *Science* 357, 306–309 (2017).
24. Zhang, H. Y. et al. The Narrowest Band Gap Ever Observed in Molecular Ferroelectrics: Hexane-1,6-diammonium Pentai dobismuth(III), *Angew. Chem.* 130, 535–539 (2018).
25. Nechache, R. et al. Bandgap Tuning of Multiferroic Oxide Solar Cells. *Nature Photonics* 9, 61–67 (2015).
26. Choi, T. et al. Switchable Ferroelectric Diode and Photovoltaic Effect in BiFeO₃ *Science*, 324, 63–66 (2009).
27. Hua, X. N. et al. A Room-Temperature Hybrid Lead Iodide Perovskite Ferroelectric. *J. Am. Chem. Soc.* 140, 12296–12302 (2018).
28. Yang, C. K. et al. The First 2D Homochiral Lead Iodide Perovskite Ferroelectrics: [R- and S-1-(4-Chlorophenyl) ethylammonium]₂PbI₄. *Adv. Mater.* 31, 1808088 (2019).
29. Liu, Y. C. et al. Surface-Tension-Controlled Crystallization for High-Quality 2D Perovskite Single Crystals for Ultrahigh Photodetection. *Matter* 1, 465–480 (2019).
30. Marin, M. & Dietrich, H. Tip-Enhanced Photovoltaic Effects in Bismuth Ferrite. *Nature Commun.* 2, 256 (2011).
31. Zhang, J. et al. Enlarging Photovoltaic Effect: Combination of Classic Photoelectric and Ferroelectric Photovoltaic Effects. *Sci. Rep.* 3, 2109 (2013).
32. Park, J. et al. Ferroelectric Photocurrent Effect in Polycrystalline Lead-Free (K_{0.5}Na_{0.5}) (Mn_{0.005}Nb_{0.995})O₃ Thin Film. *J. Am. Ceram. Soc.* 96, 146–150 (2013).
33. Bie, Y. Q. et al. Self-Powered, Ultrafast, Visible-Blind UV Detection and Optical Logical Operation based on ZnO/GaN Nanoscale *p-n* Junctions. *Adv. Mater.* 23, 649–653 (2011).
34. Zhao, R. D. et al. Boosting Photocurrent via Heating BiFeO₃ Materials for Enhanced Self-Powered UV Photodetectors. *Adv. Funct. Mater.* 30, 1906232 (2020).
35. Wu, W. W. et al. Lead Zirconate Titanate Nanowire Textile Nanogenerator for Wearable Energy-Harvesting and Self-Powered Devices. *ACS Nano* 6, 6231–6235 (2012).
36. Peng, M. Z. et al. *ACS Nano* 10, 1572–1579 (2016).
37. Bass, M. et al. Optical Rectification. *Phys. Rev. Lett.* 9, 446 (1962).
38. Giocondi, J. L. & Rohrer, G. S. Spatially Selective Photochemical Reduction of Silver on the Surface of Ferroelectric Barium Titanate. *Chem. Mater.* 13, 241–242 (2001).
39. Habicht, S. et al. Physical Adsorption on Ferroelectric Surfaces: Photoinduced and Thermal Effects. *Nanotechnology* 19, 495303 (2008).

Figures

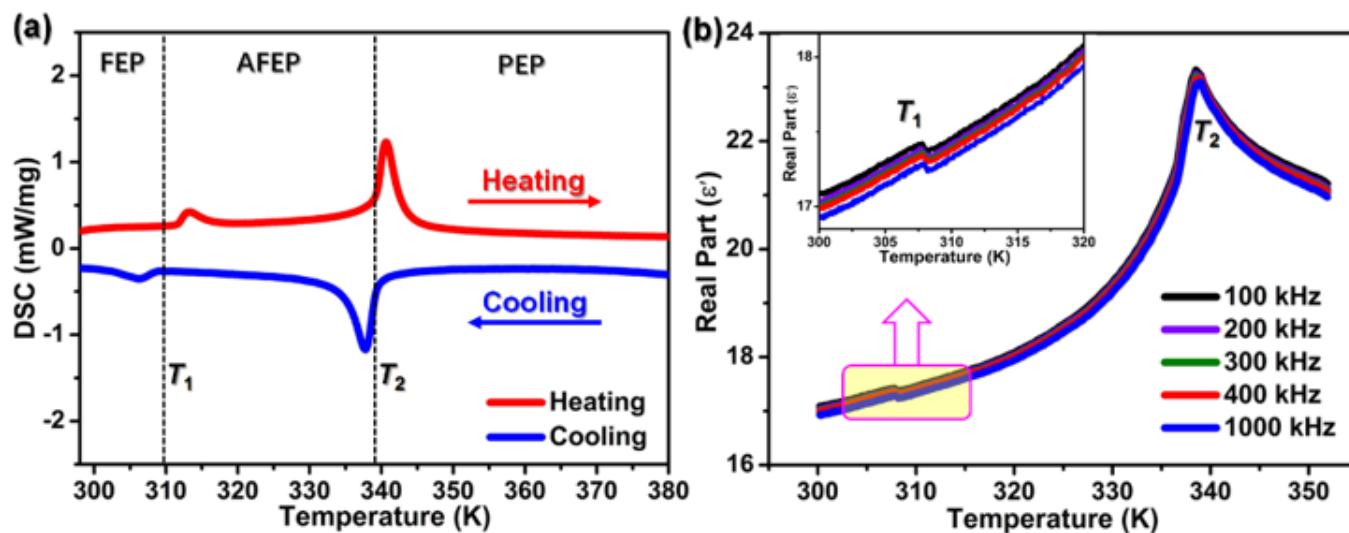


Figure 1

(a) DSC traces and (b) temperature-dependence of the dielectric constants of 1 performed on single crystals along its cFEP-axis direction upon cooling. Inset: the enlarged view of ϵ' at T_1 .

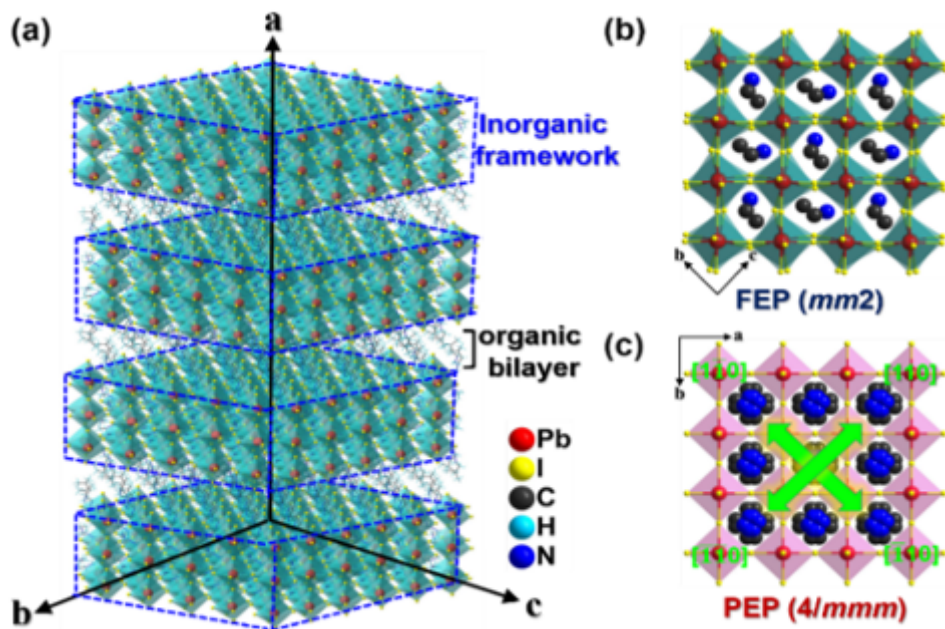


Figure 2

(a) Schematic representation of 2D Ruddlesden-Popper type structure for 1, with an alternative arrangement of inorganic trilayered perovskite frameworks containing $\{Pb3110\}_n$ and organic bilayers of isopentylammonium spacer. (b) Unit cell of 1 at FEP and (c) PEP. The polarization c -axis direction at FEP coincides with the $[110]$ -direction at PEP. There are four equivalent $[110]$ directions at PEP, as shown by the green arrowheads.

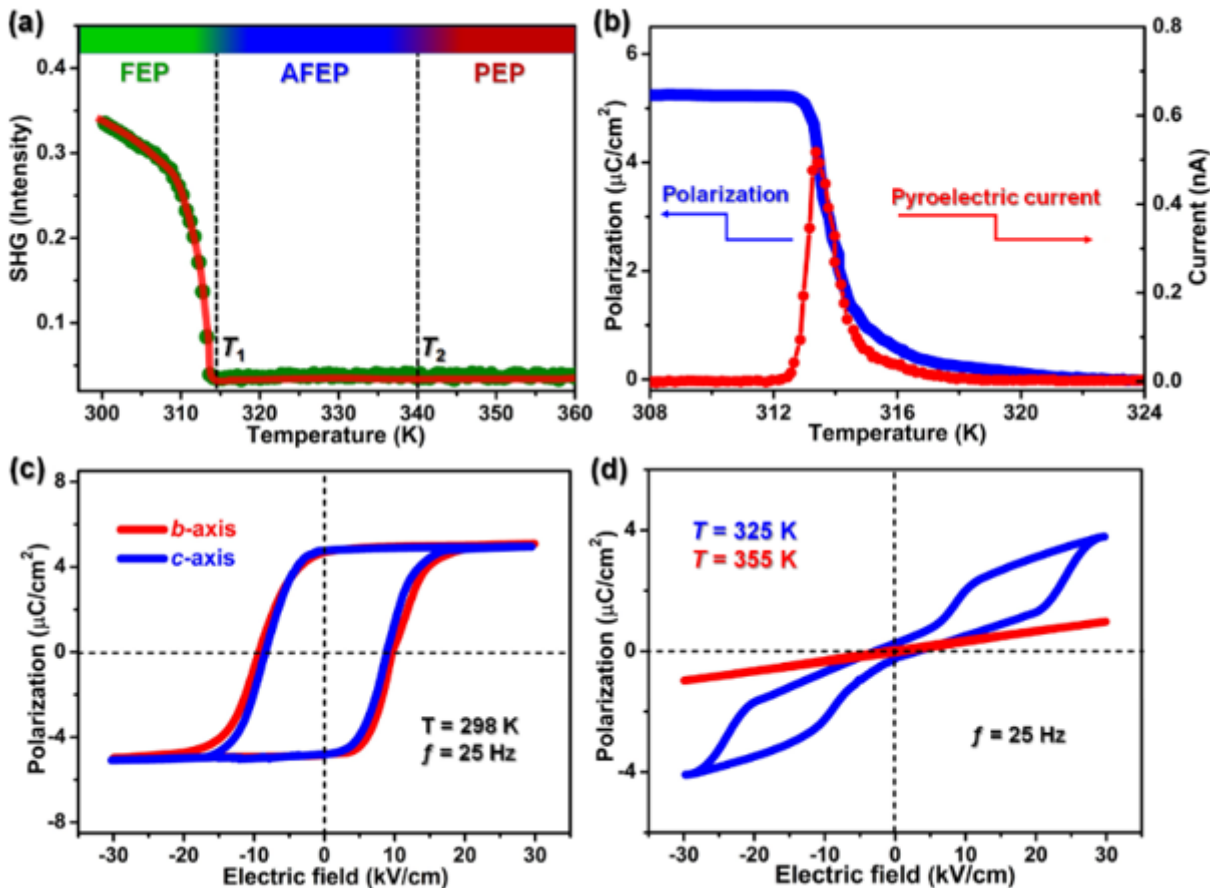


Figure 3

Ferroelectric and related properties of 1. (a) Variable-temperature SHG signals measured in the heating mode. (b) Temperature-dependent Ps deduced from the integral of pyroelectric current. (c) P-E hysteresis loops at 298 K. (d) Double P-E hysteresis loop collected at 325 K and the linear hysteresis loop at 355 K.

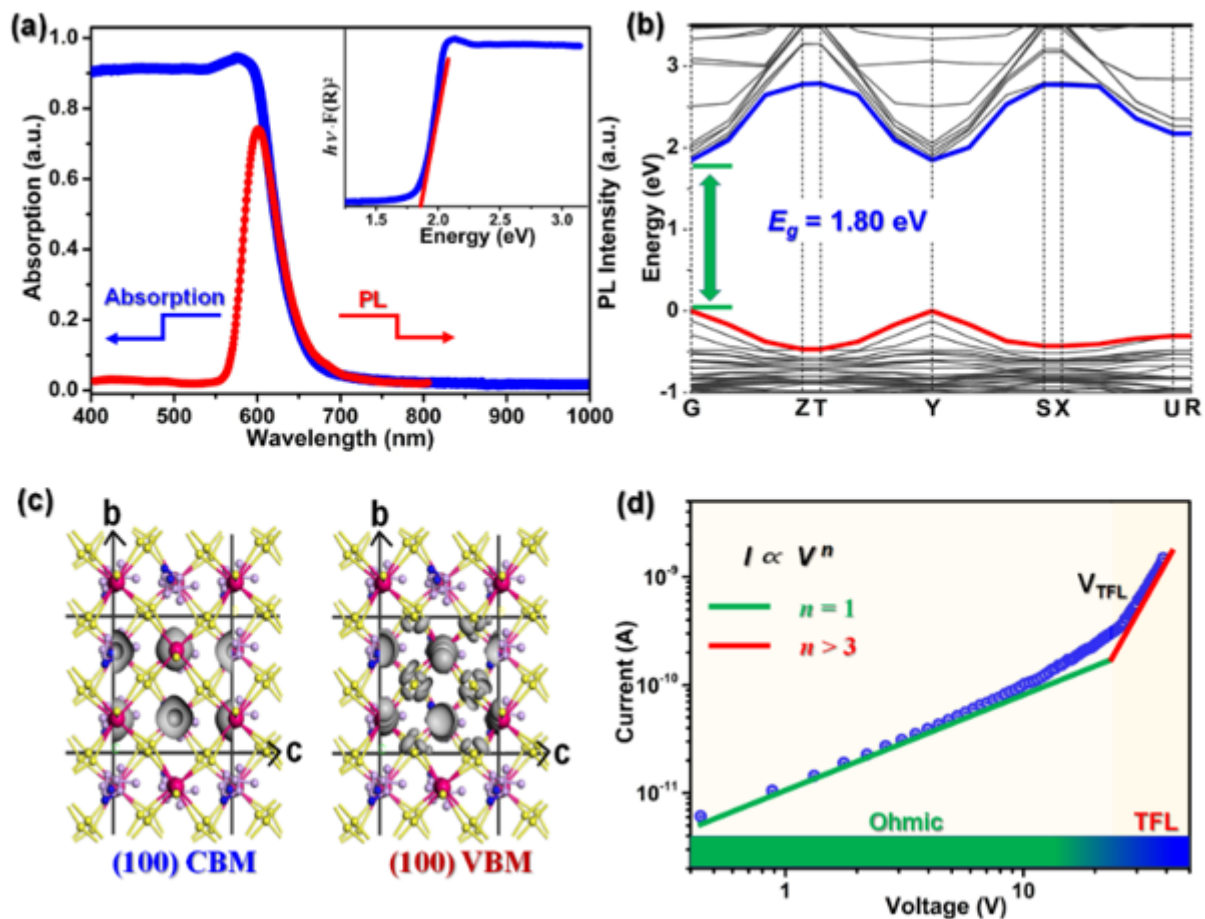


Figure 4

Optical and trap-state-density characterizations of 1. (a) Optical absorption and photoluminescence (PL) spectra. Insert: Bandgap calculated from the Tauc plot. (b) Calculated band structure. (c) Charge-density distribution of the CBM and VBM inside the crystallographic bc-plane. (d) Logarithmic dark I-V curve used for the trap-state-density measurement.

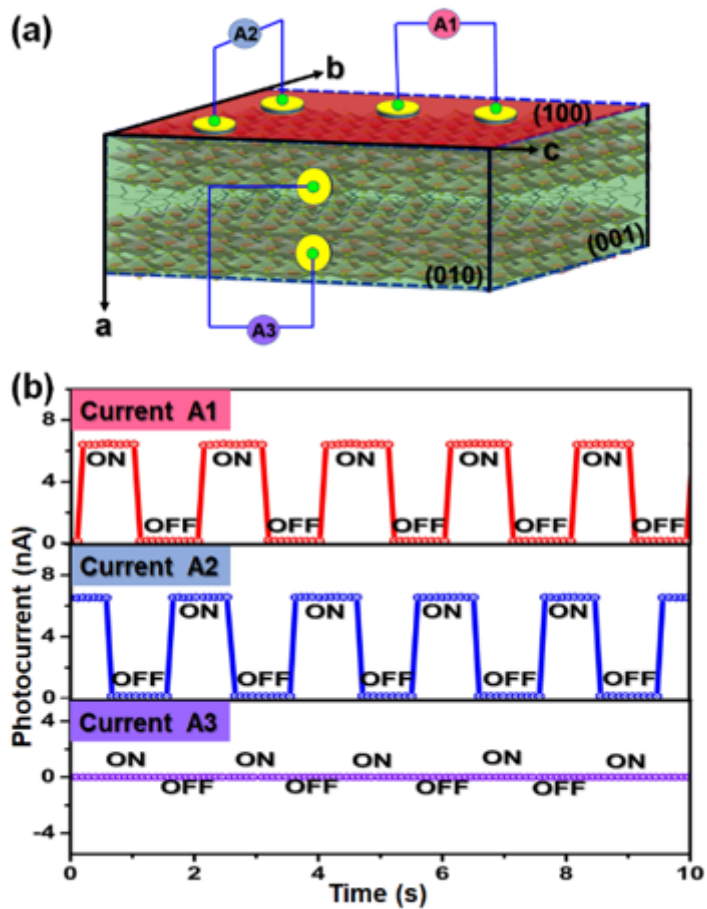


Figure 5

(a) Schematic diagram for in-plane ferroelectric BPVEs measurements with electrodes aligned parallel (A1, A2) and perpendicular (A3) to the direction of (100) plane. (b) Short-circuit photocurrent measurements in the light “on/off” cycles.

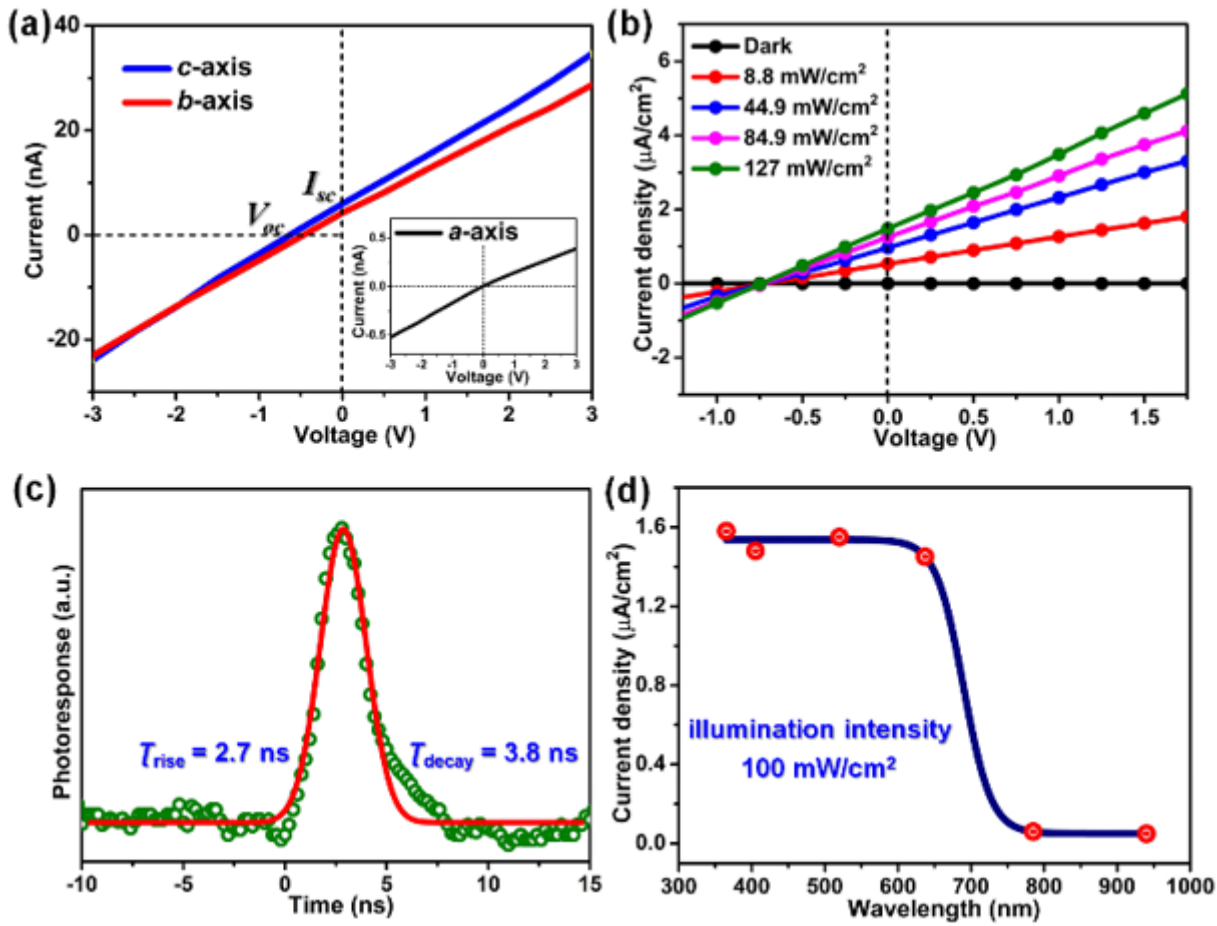


Figure 6

(a) I-V measurements of 1 measured along the b-, c-, and a-axis, respectively. (b) Photocurrent density dependence of voltage bias of 1 illuminated with a 637 nm laser. (c) Transient photoelectric responses under a nanosecond 355 nm laser. (d) Short-circuit photocurrent as a function of illumination wavelength at the zero bias.

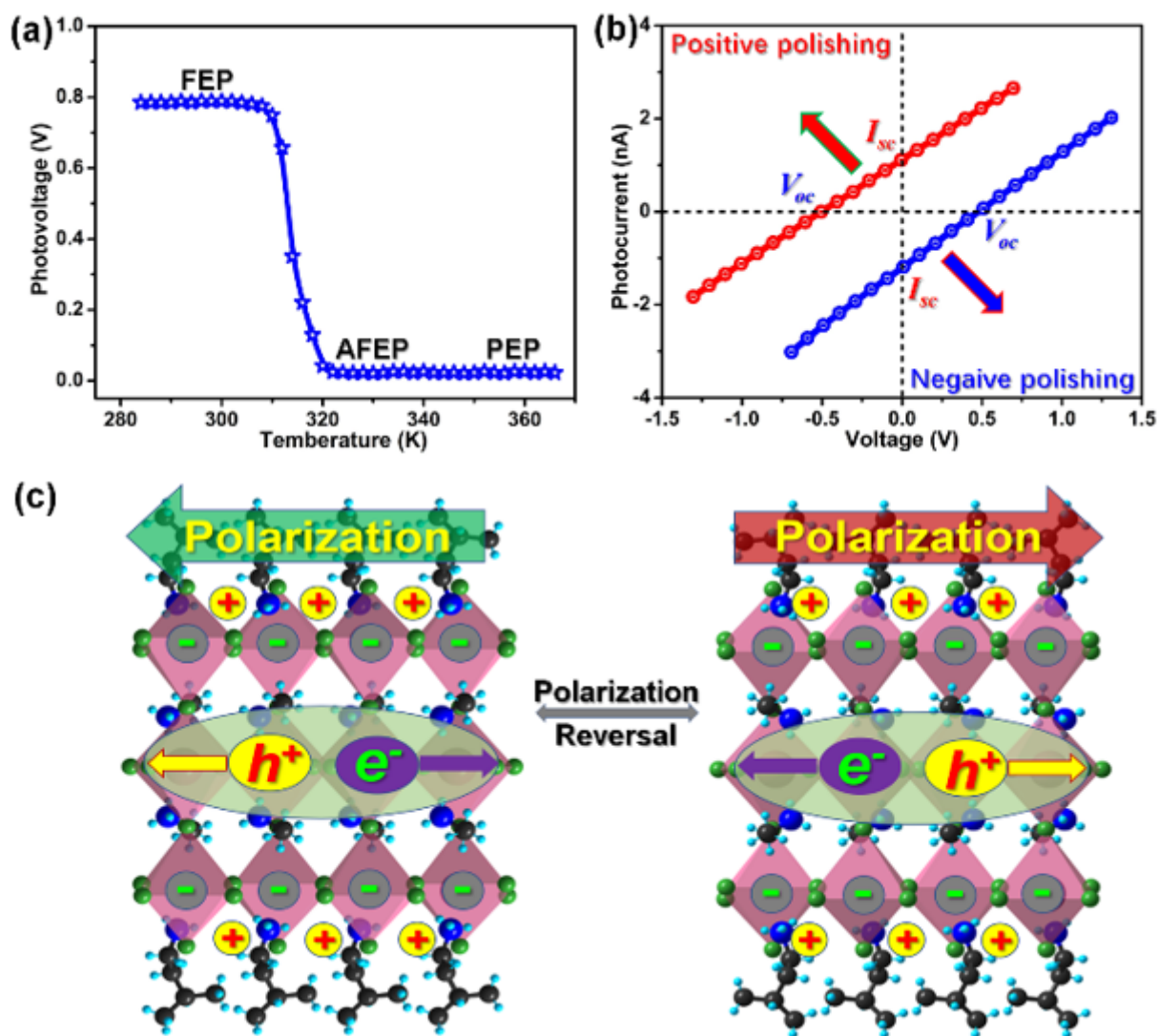


Figure 7

(a) Photovoltage dependence of temperature for 1. (b) I-V characteristics with the inversion of polarized direction. Both the direction of V_{oc} and I_{sc} can be reversed by inverting electric poling. (c) Schematic illustration of switchable photocurrent directions with polarization-related photoexcited carriers with the charge separation under positive polarization direction and negative polarization direction.

Supplementary Files

This is a list of supplementary files associated with this preprint. Click to download.

- [SupportingInformation.docx](#)